HHS Public Access

Author manuscript

Comput Biol Med. Author manuscript; available in PMC 2015 October 29.

Published in final edited form as:

Comput Biol Med. 2014 October ; 53: 65–75. doi:10.1016/j.compbiomed.2014.07.013.

A computational pipeline for quantification of mouse myocardial stiffness parameters

Øyvind Nordbø[1], **Pablo Lamata**[2], **Sander Land**[2], **Steven Niederer**[2], **Jan M. Aronsen**[3,4], **William E. Louch**[3,5], **Ivar Sjaastad**[3], **Harald Martens**[6], **Arne B. Gjuvsland**[1], **Kristin Tøndel**[2], **Hans Torp**[7], **Maelene Lohezic**[8], **Jurgen E. Schneider**[8], **Espen W. Remme**[5,9], **Nicolas Smith**[2], **Stig W. Omholt**[10], and **Jon Olav Vik**[1]

[1]Department of Mathematical Sciences and Technology, Centre for Integrative Genetics, Norwegian University of Life Sciences, P.O. Box 5003, N-1432 Ås, Norway

[2]Department of Biomedical Engineering, King's College London, St. Thomas' Hospital, Westminster Bridge Road, London SE17EH, UK

[3]Institute for Experimental Medical Research, Oslo University Hospital Ullevål and University of Oslo, Kirkeveien 166, 4th floor Building 7, 0407 Oslo, Norway

[4]Bjørknes College, Oslo, Norway

[5]KG Jebsen Cardiac Research Center and Center for Heart Failure Research, University of Oslo, 0407 Oslo, Norway

[6]Department of Engineering Cybernetics, Faculty of Information Technology, Mathematics and Electrical Engineering, Norwegian University of Science and Technology, Trondheim, Norway

[7]Department of Circulation and Medical Imaging, Faculty of Medicine, Norwegian University of Science and Technology, Postboks 8905, Medisinsk teknisk forskningssenter, NO-7491 Trondheim, Norway

[8]Radcliffe Department of Medicine, Division of Cardiovascular Medicine, University of Oxford, Welcome Trust Centre for Human Genetics, Roosevelt Drive, Oxford OX3 7BN, UK

[9]Institute for Surgical Research, Oslo University Hospital, Rikshospitalet, Oslo, Norway

[10]Faculty of Medicine, Norwegian University of Science and Technology, P.O Box 8905, N-7491 Trondheim, Norway

Abstract

The mouse is an important model for theoretical-experimental cardiac research, and biophysically based whole organ models of the mouse heart are now within reach. However, the passive material properties of mouse myocardium have not been much studied.

We present an experimental setup and associated computational pipeline to quantify these stiffness properties. A mouse heart was excised and the left ventricle experimentally inflated from 0 to 1.44 kPa in seven steps, and the resulting deformation was estimated by echocardiography and speckle

Corresponding author: Jon Olav Vik, Telephone: +47 45882998, Fax: +47 64965101, jonovik@gmail.com.

tracking. An *in silico* counterpart to this experiment was built using finite element methods and data on ventricular tissue microstructure from diffusion tensor MRI. This model assumed a hyperelastic, transversely isotropic material law to describe the force-deformation relationship, and was simulated for many parameter scenarios, covering the relevant range of parameter space. To identify well-fitting parameter scenarios, we compared experimental and simulated outcomes across the whole range of pressures, based partly on gross phenotypes (volume, elastic energy, and short- and long-axis diameter), and partly on node positions in the geometrical mesh. This identified a narrow region of experimentally compatible values of the material parameters. Estimation turned out to be more precise when based on changes in gross phenotypes, compared to the prevailing practice of using displacements of the material points. We conclude that the presented experimental setup and computational pipeline is a viable method that deserves wider application.

Keywords

Myocardial stiffness; parameter estimation; passive inflation; transversal isotropy; speckle tracking

Introduction

The passive mechanical properties of the heart wall play an important role during the filling of the ventricle; for instance, stiffening of the myocardium can lead to diastolic dysfunction and heart failure [1]. Incorporating patient-specific geometries and material properties into biomechanical models holds promise for the improved diagnosis and treatment of heart failure [2], [3]. In biomechanical models, the stress-strain relationship for myocardial tissue is described by constitutive laws whose parameters describe the material stiffness along the microstructural axes, e.g. fibre and sheet directions. Several studies have quantified passive myocardial stiffness in humans [3]–[5] and model organisms, such as the pig [6], [7], dog [8], [9] and rat [10] (see Table 1, with references). Less well studied, however, is the mouse, which is an important model organism in cardiac research. Transgenic mouse models have been extensively used in cardiac research over the last decade, where manipulation of the mouse genome has provided several novel insights in the development of cardiac disease [11]. Alterations of the myocardial properties of the heart, both in the extracellular matrix and in the cardiomyocytes, are suggested to play a major role in development of diastolic dysfunction and heart failure. Several mutations leading to heritable heart disease occur in both mouse and human [11], and the hearts have similar composition and function with regards to mechanical properties [12].

Here we propose a workflow for estimation of passive material properties of mouse myocardium by comparing computer simulations of soft tissue mechanics to observed deformation under passive inflation of an excised mouse heart. Firstly, we estimate trajectories of material points by speckle tracking of echo data through the deformation from zero to end diastolic pressure levels. This deformation is used, together with fibre structure obtained from diffusion tensor MRI, to build meshes for computer simulations. Secondly, we run model simulations and use full factorial experimental designs to cover the biological

relevant region of the parameter space for the transversely isotropic Guccione law [13]. The results show that the parameters of the constitutive law are not separately identifiable from these passive inflation measurements alone, in accordance with previous studies [14]–[16]. For the four-dimensional parameter space of the material law, we identify an elongated region of parameter combinations with nearly equivalent good fit to deformation data from passive inflation. We describe the structure of this parameter redundancy, and compare our findings with published estimates. Following a discussion of its advantages and limitations, we conclude that the presented pipeline merits wider application.

Methods

The quantification of the passive mechanical properties of the myocardium relies on mechanistic models whose parameters are tuned to reproduce the observation of a corresponding experiment [9], [14], [15]. Below we describe the passive inflation experiment with deformation measurement, MR imaging for geometric meshing, image processing and speckle tracking to estimate deformation, mechanics simulations, and comparison of experiment and simulation.

Passive inflation experiment

A single mouse was anesthetized with 5% isoflurane and sacrificed by cervical dislocation. The heart was then rapidly excised and cannulated via the aorta and mounted on a Langendorff setup (Fig. 1). The cannula was firstly placed over the level of the aortic valves, to perfuse the myocardium with cardioplegic solution of pH 7.4, 118.3 mM NaCl, 3.0 mM KCl, 4 mM $MgSO_4$, 0.2 mM $CaCl_2$, 2.4 mM KH_2PO_4, 24.9 mM $NaHCO_3$, 10 mM glucose, 2.2 mM mannitol. Some calcium was included in the superfusate since calcium-free conditions promote breakdown of gap junctions and dissociation of cardiomyocytes [17], which could cause underestimates of myocardial stiffness. The cannula was then introduced into the left ventricle, and thereafter retracted into the aorta. This technique allowed the cannula both to manipulate left ventricular pressure and to perfuse the coronary arteries; the latter was found necessary to prevent ischemia and stiffening in preliminary experiments. Pressure was increased from 0 kPa to approximately 1.44 kPa over 10 s by adjusting the height of a fluid column connected to the cannula. Deformation of the left ventricle was recorded by B-mode echocardiography (Vevo2100, VisualSonics) using a 35 MHz scan head. Three short-axis (probe mounted at the side of the ventricle) and four long-axis views (probe mounted at apex) were recorded for each pressure level (see Fig. 1 for details). Due to capillary forces in the cannula, the left ventricle pressure was not equivalent to the height of the fluid column. In a subsequent experiment, we therefore calibrated left ventricular pressure vs. fluid column height by a Samba pressure catheter (Samba 3000; Samba Sensors AB), inserted via the apex. The Samba pressure catheter was autocalibrated using the Samba memory control unit at room temperature. Proper calibration was evaluated by pressure at 0 mmHg at no height of the water column and 10 mmHg at the corresponding height of the water column.

Mesh of mouse ventricle with embedded microstructure

MR imaging: Diffusion tensor MRI (DTI) measurements of an isolated mouse heart (a different individual than the one used in the inflation experiment) embedded in 1% agarose were performed on a 9.4T horizontal bore MR system (Agilent Technologies, Santa Clara, CA) equipped with a shielded gradient system (G_{max}=1 T/m, rise time = 130 μs, inner diameter = 60 mm), using a 13 mm-diameter volume transmit/receive coil. A 3D fast spin-echo sequence was used as reported previously [18] with the following imaging parameters: TR = 1 s, number of echoes = 8, TE_{eff} = 44.25 ms, matrix size = 256×256×192, number of averages = 4, field of view 13×13×13 mm^3 (yielding a resolution of 51×51×68μm^3), maximum b-value=688 s/mm^2 (including imaging gradients and cross-terms between imaging and diffusion gradients). Eight non-collinear gradients directions were used, arranged according to an optimized scheme based on the electrostatic repulsion principle [19].

Post-processing: The fibre field was extracted from these 3D DTI data as described previously [20]. A smooth cubic Hermite mesh [21] of the left ventricle was built, and the fibre field was embedded into this mesh (see Fig. 3). The estimated transmural gradient in fibre angle was similar to previous findings [22].

Speckle tracking and estimation of 3D deformation

In ultrasound imaging, speckle pattern arises because sub-resolution scatterers interfere with the incoming ultrasound pulses. Although the reflected signal contains no information about the underlying microstructure of the tissue [23], individual pieces of tissue respond consistently to the ultrasound, and can thus be traced through a sequence of images. However, there is some uncertainty due to decorrelation of the speckle pattern between successive frames, as may be caused by out-of-plane motion, rotation, deformation, and additive thermal noise. Apart from the ultrasound gel and probe, no other external forces where applied to the ventricle.

Because the excised heart was still beating slightly, we removed images that were from the systolic phase, as identified by a high mean absolute signal difference between subsequent images. We used block-matching [23] and followed endo- and epicardial points between subsequent images through the inflation, as detailed in Appendix A. The particle paths estimated from the different slices were aligned into 3D deformed configurations for the various pressures (methods are explained in Appendix B), and a set of smooth cubic Hermite interpolated meshes (CH meshes) were then constructed combining the methods described in [21] and [24] (see Fig. 3).

Mechanical simulations

The myocardium was modelled as a hyper-elastic incompressible material [25] with homogenous, transversal isotropic properties. The framework for mechanics is described in [26]. Adopting the approach of ref. [14], we used the cubic Hermite mesh corresponding to the zero pressure configuration (CH_1, see Fig. 3) of the left ventricle (Fig. 4) as the reference configuration [27]. According to [13], the estimated stiffness parameters were not

particularly sensitive to the magnitude of the residual stress [28], which supports our approach.

We formulate the stress equilibrium equations by using the principle of virtual work on a general deformable body with initial volume V and surface area A,

$$\int_V S:\delta E dV - \int_A p_{app} F^{-T} N \cdot \delta u dA = 0. \quad (1)$$

Here S is the second Piola-Kirchhoff stress tensor and δE is the virtual Lagrangian strain tensor. p_{app} is the applied ventricular pressure acting on the endocardial surface, F^{-T} is the inverse of the transposed deformation gradient tensor, N is the normal vector for the undeformed material surface while δu is an arbitrary virtual displacement. For hyper-elastic materials, the components of the second Piola-Kirchhoff stress tensor are calculated by differentiating the strain energy function by the corresponding components of the Lagrangian strain tensor. For incompressible materials, the strains are separated into distortional and dilatational components, and we calculate the second Piola-Kirchhoff stress tensor from

$$S = \frac{\partial \hat{W}}{\partial E} - Jp(F^T F)^{-1}, \quad (2)$$

where $\hat{W}$ is the strain energy function and F is the deformation gradient tensor. The scalar p serves as a Lagrangian multiplier interpreted as the hydrostatic pressure in the material/tissue. The work done by the hydrostatic forces is zero due to the incompressibility constraint, expressed on variational form as,

$$\int_V (J-1) p dV = 0, \quad (3)$$

where J is the determinant of the deformation gradient tensor F. The stress-strain relation in hyper-elastic models follows from our assumption of a strain energy function, $\hat{W}$. The strain energy density function, $\hat{W}$, was described by the Guccione law [13]

$$\hat{W} = \frac{1}{2} a(e^Q - 1) \quad (4)$$

where

$$Q = b_1 {E_{11}}^2 + b_2({E_{22}}^2 + 2E_{23}E_{32} + {E_{33}}^2) + b_3(2E_{12}E_{21} + 2E_{13}E_{31}). \quad (5)$$

Here, a, b_1, b_2 and b_3 are material specific parameters, while E_{xy} are the various components of the Lagrangian strain tensor aligned to the underlying tissue microstructure. The subscripts indicate the microstructural directions (1 is along the fibres while 2 and 3 are orthogonal directions, normal to the fibres).

Table 1 summarizes published parameter estimates for the Guccione [13] and Costa [29] laws, showing that stiffness parameters vary across two orders of magnitude. To comprehensively cover the parameter space, simulations were performed with parameters incremented based on a log scale from the minimum to the maximum value reported in Table 1.

For the 4 Guccione law parameters, we used a full factorial design with eight levels, resulting initially in8^4 = 4096 parameter sets. For each parameter set, the simulation model was run for the same pressure steps as in the experiment (eleven levels ranging from zero to 1.44 kPa).

We applied boundary conditions constraining the basal plane to not move in the z-direction, which should correspond well to the experimental setup where the heart was attached to the cannula through the aortic valve. Additional Dirichlet boundary conditions to avoid whole-body rotation/translation are shown in Fig. 4.

Inside the cavity, we assumed a homogeneous internal pressure, which should be a reasonable assumption due to the low velocity of the flow. In the model we neglected the forces between the ultrasound gel and the heart, which is the simplest possible assumption until such forces are measured. As in previous published studies of similar setups [14], we also assumed that the influence from the right ventricle was negligible.

Comparison of measured and simulated deformations

In both the simulations and the measurements, the shape of the heart ventricle at a given pressure is represented by node positions and an associated cubic Hermite interpolation of the surfaces between nodes. We tried two different objective functions for comparison of experimental and simulated deformation, restricting the computation to the most biologically relevant pressure range [30], > 0.2 kPa.

1. Comparison of positions for all endocardial and epicardial nodes in the CH mesh. The criterion for good fit was the L2 norm between experimental and simulated node position, averaged over the relevant pressures M and nodes N in the mesh,

$$\Omega_1=\frac{1}{MN}\sum_{m=1}^{M}\sum_{n=1}^{N}\left(\sqrt{(x_{sim}-x_{\exp})^2+(y_{sim}-y_{\exp})^2+(z_{sim}-z_{\exp})^2}\right)_{mn} \quad (6)$$

2. Comparison of K = 4 aggregated phenotypes (change in Volume (ΔV), short and long axis diameter (ΔS_a and ΔL_a), and elastic energy ($\int P\mathrm{d}V$, computed as the integral of the pressure-volume curve). For each phenotypic variable, the difference between simulation and experiment is nondimensionalized as a proportion of the respective experimental value. Then, each variable is weighted equally in averaging over the K phenotypes and M relevant pressures:

$$\Omega_2=\frac{1}{MK}\sum_{m=1}^{M}\sum_{k=1}^{K}\mathrm{abs}\left(\frac{\Phi_{sim}-\Phi_{\exp}}{\Phi_{\exp}}\right)_{mk} \quad (7)$$

These objective functions were computed for all simulated parameter scenarios, and we identified the parameter regions that corresponded to low values of each objective function. The identified region of the parameter space was further analyzed by manually selecting new parameter limits and running new simulations for a full factorial design over the new parameter regions. We did this in an iterative way (3 times), and got an overview of the landscape of the parameter space and were able to see the correlation between estimated parameters.

We evaluated the ability of each objective function to precisely estimate parameters (i.e. identify a small set of well-fitting parameter scenarios) by asking "how many parameter scenarios lie within a given % increase from the optimal value (least lack-of-fit) of the objective function?" This is valid because both objective functions have a meaningful absolute zero point.

Results

Experimental deformation

The deformation of the experimentally manipulated heart was estimated by speckle tracking of four long-axis and three short-axis image sequences. The free wall generated larger longitudinal strains than the septum, causing the apex to tilt towards the septum during the inflation (Fig. 2). The pressure-volume relationship was quite linear within the interval of applied pressures (Fig. 7a), in agreement with previous *in vivo* work [31], [32]. The mesh corresponding to zero and maximum pressures are shown in Fig. 4.

Comparison of simulated vs. experimental deformation

The objective function based on aggregated phenotypes (equation (7)) was more selective than the one based on node positions (equation (6)), in terms of identifying some parameter scenarios as better fitting than others (Fig. 5). For example, the number of parameter scenarios within a 50% increase from the minimum of the objective functions (6) and (7) was 5729 and 65, respectively. Likewise, the contrast between Fig. 6 and Fig. 7a shows how the scenarios selected by the latter criterion give a much tighter match to the observed inflation trajectory. Furthermore, the objective function (6) tended to select scenarios with much lower compliance than observed in the experiment (Fig. 6) and worse fits for whole organ phenotypes (Fig. 7). Subsequent analyses were therefore based on the objective function in equation (7). Especially for the volume, short axis and elastic energy, the model was able to capture the essential dynamics.

Correlation structure of well-fitting parameter combinations

Well-fitting parameter combinations (i.e. those with a low value of the objective function) showed considerable variation along all individual parameter axes, though there were clear patterns of covariation among parameters (Fig. 8). Similar to the finding in [24], the well-fitting parameter scenarios tended to lie nearly along a straight line in the space of ($\log a$, $\log(b_1+b_2+b_3)$).

The estimated overall stiffness parameter a was clearly bounded from below, while the values of the b were bounded from above. Conditional on a value for a, the b_1 and b_2 parameters were also bounded from below, but the optimal estimate of b_3 approached parameter regions with bad convergence of the mechanics solver. The tissue was stiffer along the fibres than in the directions orthogonal to the fibres (b_1 =5.0, b_2 =3.7, b_3 =2.6), with b_2 more tightly constrained than b_1 and b_3 (Table 1, Fig. 8). Although the point estimate appears comfortably inside the explored parameter region as viewed in the projections in Fig. 8, there were convergence problems for some of the parameter scenarios adjoining the best-fitting one as viewed in more than two parameter dimensions. Therefore, we cannot conclude whether the material parameters would be uniquely identifiable with a more robust numerical integration solver.

Discussion

There are several advantages to the experimental and computational pipeline presented here. Echocardiography is simple to use during pressure manipulation of excised hearts and is faster than tagged MRI (as used in e.g. [14]), thus reducing problems with rigor mortis. Furthermore, it can follow internal material points over the entire geometry [9], unlike the method of video recordings of epicardial markers (used by [33]). Passive inflation experiments avoid the sectioning of tissue required for uni-axial and biaxial material testing [34], which would disrupt the microstructure and influence the material properties. However, this limits the possibility of experimentally inducing shear forces as described by [35]. [8] argue that passive inflation produces insufficient transverse shear strain to quantify the material properties in those directions, and therefore developed an epicardial suction setup for isolated arrested hearts. However, our results indicate that the relevant parameter (b_3) is constrained from above (Fig. 8), but shows larger relative uncertainty than the other b parameters in the Guccione law (4)–(5).

Our numerical experiments enable parameter estimation and an overview of the structure of parameter uncertainty across a bounding box of all previously published parameter estimates (Table 1; see Supplementary Figure S1 for a visual comparison of the corresponding stress-strain relationships). The simultaneous estimation of parameters is an improvement over one-at-a-time optimization, and highlights the possibility that many empirical data sets may not be able to support the complexity of commonly used models and material laws [24], [36]. The robustness of an exhaustive search comes with the associated computational cost of a wide sweep of parameters, as compared with other approaches [4], [24], [37], [38].

The definition of an adequate objective function to compare data and model is critical for a data assimilation method. Both data and model are limited by acquisition issues and assumptions, respectively, and a suitable choice of the space to compare them is required. Parameters were easier to identify using aggregate measures of cardiac deformation, rather than the more detailed node positions, for the goodness-of-fit criterion (objective function). This may reflect an inability of our model to mimic certain deformations that occurred in the experimental data, particularly a bending due to larger longitudinal strains in the free ventricular wall than the septum during inflation (Fig. 3, bottom), or circumferential variation in material stiffness, violating our assumption of homogeneity. Other possible

causes originate in the experimental data, a 3D reconstruction of 2D observations that is subject to misregistration and out-of-plane errors. Regardless of the cause, our results suggest that a gross description of mechanical deformation introduces the benefit of a more relevant and robust comparison between data and model.

As opposed to the traditional and more intuitive direct use of displacement fields for the objective function [9], [24], recent works have explored the use of integral deformation metrics [37], or advanced mathematical frameworks (using the concept of currents) [39]. Our proposed aggregated phenotypic metric is a simple and effective solution, and offers an intuitive interpretation of where the agreement and disagreement occurs. Preliminary results with our echo data, not reported here, showed that the inclusion of twist (defined as the difference in rotation between base and apex as done clinically [40]) in the objective function was detrimental, probably due to a combination of imaging acquisition and analysis limitations. Further research is needed to optimise the definition of the objective functional, and to analyse the comparative performance of the different alternatives.

Because the excised heart kept beating a little throughout the experiment (see “Speckle tracking” in Methods), despite perfusion with cardioplegic solution, and we were unable to measure the calcium level inside the heart, we cannot be sure about our assumption that there were no active forces. This assumption greatly simplifies the decoupling of active and passive relaxation processes [15], but may overestimate the stiffness of the tissue. On the positive side, the residual heartbeat confirmed that the excised heart was still capable of contraction, and so its material properties remained similar to *in vivo*.

Our experiment showed that the fibre stress-strain relationship for the mouse left ventricle was quite linear over a biologically relevant range of pressures (Fig. S1). This brings challenges in identifying, separately from the overall stiffness a, the b parameters that pertain to curvature in the material law (Fig. 8, [24]). However, in contrast to [24], we find that a is well bounded from below while the b’s are bounded from above: No parameter scenarios with low a or very high b’s could be made to match the data well (Fig. 8).

The mouse myocardium was found to be stiffer along the fibres than normal to the fibres, which is in agreement with the findings in other model organisms [6]–[10]. The value of b_1 was considerably higher than b_2 and b_3, in agreement with findings in *in vivo* sheep and human hearts [15], [41] and in tissue blocks of pig heart [7]. The stiffness parameters estimated in this work describe a relatively soft material (low stress-strain relationships) compared with most of the literature, and is most similar to the material properties found in a similar experiment on rat hearts [10].

Complementary experiments are needed to better constrain the material parameters of this law. We inflated the ventricle from 0 to 1.44 kPa, i.e. within the normal diastolic pressure range. In this range the stress (or pressure) vs. deformation relationship was relatively linear, while the nonlinear behavior occurs at higher pressures. The estimated parameters capture the passive material properties for normal diastolic pressures in a healthy specimen, but extrapolation outside this range, for example for the study of increased filling pressures, will require further characterization.

Several future refinements are possible in this parameter estimation workflow. Better speckle tracking would improve the ability to find regional differences in material passive properties by following material points in a Lagrangian, moving frame of reference, as suggested for tagged MRI by [16]. Other challenges include the aligning of 2D data into 3D geometries. Misalignment may cause spurious bulging in the estimated deformation of the apex region (Fig. 4), and is probably one of the main reasons for the lack of fit between the simulated and experimental deformation data on a nodal basis (eq. (6) and Fig. 5). Manual interactions could be reduced, facilitating e.g. the study of individual variation, by automating the selection of valid end diastolic frames from the echocardiographic recordings. Also, mesh construction might benefit from being constrained by incompressibility [42]; our current meshes differed in volume by 15% from the start to the end of filling. Complementary experiments are needed to uniquely constrain the material parameters of this law. In particular, the application of higher pressures, e.g. of relevance to hypertension, might bring out nonlinearities in the force-deformation relationship that would constrain the possible parameter combinations.

We have demonstrated the feasibility of quantifying mouse myocardial stiffness using the experimental setup and associated computational pipeline described above, and found that it is a viable method that deserves wider application. A better knowledge of passive properties would shed light on diastolic dysfunction and is an important step towards understanding diastolic heart failure in mouse and human.

Supplementary Material

Refer to Web version on PubMed Central for supplementary material.

Acknowledgments

This work was funded by the Research Council of Norway under the eVITA programme, project number 178901/V30 and by the Virtual Physiological Rat project funded through NIH grant P50-GM094503. NOTUR, the Norwegian metacenter for computational science, provided computing resources under project nn4653k. JES is a BHF Senior Basic Science Research Fellow, and acknowledges funding from the Biotechnology & Biological Sciences Research Council (BB/I012117/1).

Glossary

LVP	Left Ventricular Pressure
MVO	Mitral Valve Opening
ED	End Diastole
ES	End Systole
PV	Pressure Volume

References

1. Borlaug BA, Kass DA. Mechanisms of Diastolic Dysfunction in Heart Failure. Trends in Cardiovascular Medicine. Nov; 2006 16(8):273–279. [PubMed: 17055383]

2. Fenton FH, Luther S, Cherry EM, Otani NF, Krinsky V, Pumir A, Bodenschatz E, Gilmour RF. Termination of Atrial Fibrillation Using Pulsed Low-Energy Far-Field Stimulation. Circulation. 2009; 120(6):467–476. [PubMed: 19635972]
3. Xi J, Lamata P, Niederer S, Land S, Shi W, Zhuang X, Ourselin S, Duckett SG, Shetty AK, Rinaldi CA, Rueckert D, Razavi R, Smith NP. The estimation of patient-specific cardiac diastolic functions from clinical measurements. Medical Image Analysis. Feb; 2013 17(2):133–146. [PubMed: 23153619]
4. Delingette H, Billet F, Wong KCL, Sermesant M, Rhode K, Ginks M, Rinaldi CA, Razavi R, Ayache N. Personalization of Cardiac Motion and Contractility From Images Using Variational Data Assimilation. IEEE Transactions on Biomedical Engineering. Jan; 2012 59(1):20–24. [PubMed: 21712158]
5. Sermesant M, Moireau P, Camara O, Sainte-Marie J, Andriantsimiavona R, Cimrman R, Hill DLG, Chapelle D, Razavi R. Cardiac function estimation from MRI using a heart model and data assimilation: Advances and difficulties. Medical Image Analysis. Aug; 2006 10(4):642–656. [PubMed: 16765630]
6. Augenstein KF, Cowan BR, LeGrice IJ, Young AA. Estimation of cardiac hyperelastic material properties from MRI tissue tagging and diffusion tensor imaging. Med Image Comput Comput Assist Interv. 2006; 9(Pt 1):628–635. [PubMed: 17354943]
7. Schmid H, O'Callaghan P, Nash M, Lin W, LeGrice I, Smaill B, Young A, Hunter P. Myocardial material parameter estimation. Biomechanics and Modeling in Mechanobiology. Jun; 2008 7(3): 161–173. [PubMed: 17487519]
8. Okamoto R, Moulton M, Peterson S, Li D, Pasque M, Guccione J. Epicardial suction: A new approach to mechanical testing of the passive ventricular wall. J Biomech Eng-Trans ASME. Oct; 2000 122(5):479–487.
9. Wang VY, Lam HI, Ennis DB, Cowan BR, Young AA, Nash MP. Modelling passive diastolic mechanics with quantitative MRI of cardiac structure and function. Med Image Anal. Oct; 2009 13(5):773–784. [PubMed: 19664952]
10. Omens JH, MacKenna DA, McCulloch AD. Measurement of strain and analysis of stress in resting rat left ventricular myocardium. Journal of Biomechanics. Jun; 1993 26(6):665–676. [PubMed: 8514812]
11. Morita H, Seidman J, Seidman CE. Genetic causes of human heart failure. J Clin Invest. Mar; 2005 115(3):518–526. [PubMed: 15765133]
12. Georgakopoulos D, Mitzner WA, Chen CH, Byrne BJ, Millar HD, Hare JM, Kass DA. In vivo murine left ventricular pressure-volume relations by miniaturized conductance micromanometry. Am J Physiol Heart Circ Physiol. Apr; 1998 274(4):H1416–H1422.
13. Guccione JM, McCulloch AD, Waldman LK. Passive Material Properties of Intact Ventricular Myocardium Determined From a Cylindrical Model. J Biomech Eng. Feb; 1991 113(1):42–55. [PubMed: 2020175]
14. Augenstein KF, Cowan BR, LeGrice IJ, Nielsen PMF, Young AA. Method and Apparatus for Soft Tissue Material Parameter Estimation Using Tissue Tagged Magnetic Resonance Imaging. J Biomech Eng. Feb; 2005 127(1):148–157. [PubMed: 15868797]
15. Xi J, Lamata P, Niederer S, Land S, Shi W, Zhuang X, Ourselin S, Duckett SG, Shetty AK, Rinaldi CA, Rueckert D, Razavi R, Smith NP. The estimation of patient-specific cardiac diastolic functions from clinical measurements. Med Image Anal. Oct.2012
16. Xi J, Lamata P, Lee J, Moireau P, Chapelle D, Smith N. Myocardial transversely isotropic material parameter estimation from in-silico measurements based on a reduced-order unscented Kalman filter. Journal of the Mechanical Behavior of Biomedical Materials. Oct; 2011 4(7):1090–1102. [PubMed: 21783118]
17. Muir AR. The effects of divalent cations on the ultrastructure of the perfused rat heart. Journal of anatomy. 1967; 101(Pt 2):239. [PubMed: 6040076]
18. Hales PW, Burton RAB, Bollensdorff C, Mason F, Bishop M, Gavaghan D, Kohl P, Schneider JE. Progressive changes in T1, T2 and left-ventricular histo-architecture in the fixed and embedded rat heart. NMR Biomed. Aug; 2011 24(7):836–843. [PubMed: 21834007]

19. Jones DK, Horsfield MA, Simmons A. Optimal strategies for measuring diffusion in anisotropic systems by magnetic resonance imaging. Magn Reson Med. Sep; 1999 42(3):515–525. [PubMed: 10467296]

20. Lamata, P.; Niederer, S.; Plank, G.; Smith, N. Generic conduction parameters for predicting activation waves in customised cardiac electrophysiology models. Proceedings of the First international conference on Statistical atlases and computational models of the heart, and international conference on Cardiac electrophysiological simulation challenge; Berlin, Heidelberg. 2010. p. 252-260.

21. Lamata P, Niederer S, Nordsletten D, Barber DC, Roy I, Hose DR, Smith N. An accurate, fast and robust method to generate patient-specific cubic Hermite meshes. Medical Image Analysis. Dec; 2011 15(6):801–813. [PubMed: 21788150]

22. LeGrice IJ, Smaill BH, Chai LZ, Edgar SG, Gavin JB, Hunter PJ. Laminar structure of the heart: ventricular myocyte arrangement and connective tissue architecture in the dog. Am J Physiol. Aug; 1995 269(2 Pt 2):H571–582. [PubMed: 7653621]

23. Crosby J, Amundsen BH, Hergum T, Remme EW, Langeland S, Torp H. 3-D Speckle Tracking for Assessment of Regional Left Ventricular Function. Ultrasound in Medicine & Biology. Mar; 2009 35(3):458–471. [PubMed: 19056164]

24. Xi, J.; Lamata, P.; Shi, W.; Niederer, S.; Land, S.; Rueckert, D.; Duckett, SG.; Shetty, AK.; Rinaldi, CA.; Razavi, R.; Smith, N. An Automatic Data Assimilation Framework for Patient-Specific Myocardial Mechanical Parameter Estimation. In: Metaxas, DN.; Axel, L., editors. Functional Imaging and Modeling of the Heart. Vol. 6666. Berlin, Heidelberg: Springer Berlin Heidelberg; 2011. p. 392-400.

25. Bonet, J.; Wood, RD. Nonlinear Continuum Mechanics for Finite Element Analysis. 2. Cambridge University Press; 2008.

26. Land S, Niederer SA, Smith NP. Efficient computational methods for strongly coupled cardiac electromechanics. IEEE Trans Biomed Eng. May; 2012 59(5):1219–1228. [PubMed: 21303740]

27. Nordsletten DA, Niederer SA, Nash MP, Hunter PJ, Smith NP. Coupling multi-physics models to cardiac mechanics. Progress in Biophysics and Molecular Biology. Jan; 2011 104(1–3):77–88. [PubMed: 19917304]

28. Omens J, Fung Y. Residual strain in rat left ventricle. Circ Res. Jan; 1990 66(1):37–45. [PubMed: 2295143]

29. Costa KD, Holmes JW, McCulloch AD. Modelling cardiac mechanical properties in three dimensions. Philosophical Transactions of the Royal Society of London Series A: Mathematical, Physical and Engineering Sciences. Jun; 2001 359(1783):1233–1250.

30. Pacher P, Nagayama T, Mukhopadhyay P, Bátkai S, Kass DA. Measurement of cardiac function using pressure–volume conductance catheter technique in mice and rats. Nat Protoc. 2008; 3(9): 1422–1434. [PubMed: 18772869]

31. Land S, Louch WE, Niederer SA, Aronsen JM, Christensen G, Sjaastad I, Sejersted OM, Smith NP. Beta-Adrenergic Stimulation Maintains Cardiac Function in Serca2 Knockout Mice. Biophysical Journal. Mar; 2013 104(6):1349–1356. [PubMed: 23528094]

32. Cingolani OH, Kass DA. Pressure-volume relation analysis of mouse ventricular function. AJP: Heart and Circulatory Physiology. Dec; 2011 301(6):H2198–H2206. [PubMed: 21926344]

33. McCulloch AD, Smaill BH, Hunter PJ. Regional left ventricular epicardial deformation in the passive dog heart. Circulation Research. Apr; 1989 64(4):721–733. [PubMed: 2702734]

34. Yin FCP, Strumpf RK, Chew PH, Zeger SL. Quantification of the mechanical properties of noncontracting canine myocardium under simultaneous biaxial loading. Journal of Biomechanics. 1987; 20(6):577–589. [PubMed: 3611134]

35. Dokos S, Smaill BH, Young AA, LeGrice IJ. Shear properties of passive ventricular myocardium. Am J Physiol Heart Circ Physiol. Dec; 2002 283(6):H2650–2659. [PubMed: 12427603]

36. Gutenkunst RN, Waterfall JJ, Casey FP, Brown KS, Myers CR, Sethna JP. Universally Sloppy Parameter Sensitivities in Systems Biology Models. PLoS Computational Biology. 2007; 3:189.

37. Marchesseau S, Delingette H, Sermesant M, Cabrera-Lozoya R, Tobon-Gomez C, Moireau P, Figueras i Ventura RM, Lekadir K, Hernandez A, Garreau M, Donal E, Leclercq C, Duckett SG, Rhode K, Rinaldi CA, Frangi AF, Razavi R, Chapelle D, Ayache N. Personalization of a cardiac

electromechanical model using reduced order unscented Kalman filtering from regional volumes. Medical Image Analysis. Oct; 2013 17(7):816–829. [PubMed: 23707227]

38. Moireau P, Chapelle D, Tallec PL. Joint state and parameter estimation for distributed mechanical systems. Computer Methods in Applied Mechanics and Engineering. Jan; 2008 197(6–8):659–677.
39. Imperiale, A.; Routier, A.; Durrleman, S.; Moireau, P. Functional Imaging and Modeling of the Heart. Springer; 2013. Improving efficiency of data assimilation procedure for a biomechanical heart model by representing surfaces as currents; p. 342-351.
40. Kowallick JT, Edelmann F, Lotz J, Lamata P, Schuster A. Imaging Diastolic Dysfunction with Cardiovascular Magnetic Resonance. Journal of Cardiology and Therapy. Oct; 2014 1(4):58–64.
41. Walker JC, Ratcliffe MB, Zhang P, Wallace AW, Fata B, Hsu EW, Saloner D, Guccione JM. MRI-based finite-element analysis of left ventricular aneurysm. Am J Physiol Heart Circ Physiol. Aug; 2005 289(2):H692–H700. [PubMed: 15778283]
42. Shi W, Zhuang X, Wang H, Duckett S, Luong DVN, Tobon-Gomez C, Tung K, Edwards PJ, Rhode KS, Razavi RS, Ourselin S, Rueckert D. A comprehensive cardiac motion estimation framework using both untagged and 3-D tagged MR images based on nonrigid registration. IEEE Trans Med Imaging. Jun; 2012 31(6):1263–1275. [PubMed: 22345530]
43. MATLAB, version 7.7.0 (R2008b). Natick, Massachusetts: The MathWorks Inc;
44. Sun K, Stander N, Jhun CS, Zhang Z, Suzuki T, Wang GY, Saeed M, Wallace AW, Tseng EE, Baker AJ, Saloner D, Einstein DR, Ratcliffe MB, Guccione JM. A Computationally Efficient Formal Optimization of Regional Myocardial Contractility in a Sheep with Left Ventricular Aneurysm. J Biomech Eng. Nov.2009 131(11):111001. [PubMed: 20016753]
45. Land S, Niederer S, Aronsen JM, Espe EKS, Zhang L, Louch WE, Sjaastad I, Sejersted OM, Smith N. An Analysis of Deformation Dependent Electromechanical Coupling in the Mouse Heart. J Physiol. May.2012
46. Usyk T, Mazhari R, McCulloch AD. Effect of Laminar Orthotropic Myofiber Architecture on Regional Stress and Strain in the Canine Left Ventricle. Journal of Elasticity. 2000; 61
47. Schmid H, Nash MP, Young AA, Hunter PJ. Myocardial Material Parameter Estimation---A Comparative Study for Simple Shear. J Biomech Eng. Oct; 2006 128(5):742–750. [PubMed: 16995761]
48. Nordsletten D, McCormick M, Kilner PJ, Hunter P, Kay D, Smith NP. Fluid–solid coupling for the investigation of diastolic and systolic human left ventricular function. International Journal for Numerical Methods in Biomedical Engineering. Jul; 2011 27(7):1017–1039.

Appendix A: Speckle tracking

Two-dimensional particle paths can be estimated from a series of images by block-matching [23]. The algorithm compares a region of the current image with nearby regions in the next image, finding the best-matching displacement by optimizing some matching criterion. This is repeated for each region of interest in the current image, for example centred on manually chosen landmarks to be tracked.

Each series consisted of approximately 300 images (long-axis: 512×384 pixels; short-axis: 512×472 pixels; pixel size 0.0234 mm). However, the heart was still beating a little during the experiment, whereas our focus was on passive mechanics only. We therefore removed systolic images before speckle tracking, identifying these images by their large mean absolute signal intensity difference between subsequent images. Because the sampling rate was high relative to the rate of displacement, we subsampled the data to every third image to avoid round off problems with zero displacements. The speckle tracking algorithm was implemented in Matlab ([43]) as follows:

- We chose limits for the search algorithm, consisting of the size of the matching kernel window and the maximum allowed displacements. Kernel windows were 17×31 and 9×17 pixels for long- and short-axis images, respectively. The maximum allowed displacements between two subsequent images were 2 pixels (in x and y direction) for long-axis and 3 pixels for short-axis images.
- The ventricular wall was more visible and easier to segment from the high pressure images. We therefore selected material points along the inner and outer surface of the ventricle for the image corresponding to maximal pressure, and worked backwards from high to low pressure images. The selected material points were used as central points for block matching between subsequent images in the following automatic procedure.
  - The ventricle in the current image was masked based on the position of the material points in the preceding image (echo intensity was set to NaN outside the ventricle).
  - The displacement for each material point in the current image was estimated by matching the neighbourhood of the material point against candidate regions in the next image, minimizing the mean absolute difference between the sub-images.
  - Due to considerable noise, especially in the basal region in the long axis images, we imposed additional constraints on the deformation:
    - The material points closest to the base were allowed to move only in horizontal direction and the outward radial search region was reduced.
    - The local wall thickness was measured. If the wall thickness was shrinking compared with the max pressure image, the material points on the inner wall were moved inwards, normal to the surface of the outer wall.
  - The displacements were smoothed using a cubic spline. (Displacements from short axis images were converted to polar coordinates before smoothing).
  - The coordinate position of each material point was updated, based on its estimated displacement, before the next image was analysed by block-matching.

Appendix B: From 2D particle paths to 3D deformation

The individual 2D particle paths were smoothed over time and interpolated so we could estimate the position of each 2D material point for any specified LVP. We used the long-axis images to find displacement in longitudinal and radial direction, while circumferential displacements were obtained from the short-axis images. The short-axis images also contain information about the radial movement, but this was not utilized because the out-of-plane movement is larger for these images than for long-axis images. The long-axis images were centred, based on the centre of mass of the basal points in the zero pressure images, and rotated about the z-axis (0°, 45°, 90° and 135°) to correspond to the experimental views (see

Fig. 1 a). The apical points were defined as a weighted average of the most apical points from the different long-axis slices. The short-axis images were aligned to match the long-axis images with respect to the free wall and the septum. The most apical short-axis image was aligned with the long-axis images in the z-direction, so that the inner diameters of the long- and short-axis images were identical in the maximum pressure configuration. The circumferential displacements of all nodes were then interpolated in the z-direction between the short-axis slices by using a cubic spline (we required zero circumferential displacement in the base, in accordance to the experimental setup). The nodes were then used as nodes in a triquadratic interpolated mesh, and estimated 3D-displacements were used to calculate the configuration for each pressure level (see Fig. 3).

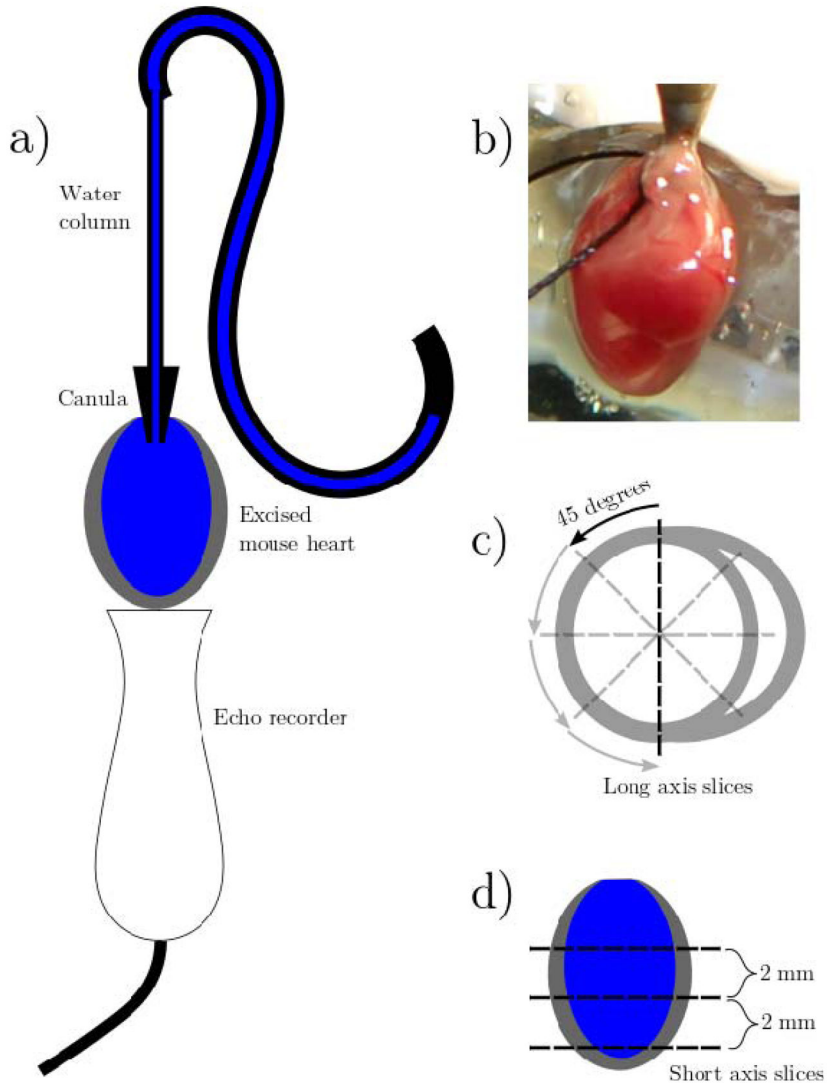

Fig. 1.

a) Sketch of experimental setup for echo measurements; b) Mouse heart with cannula and echo recorder; c) placement of long-axis views of the heart (45 degree rotation between views, probe placed apically to the heart); d) placement of short-axis views (2 mm vertical spacing, probe placed at the side of the heart)

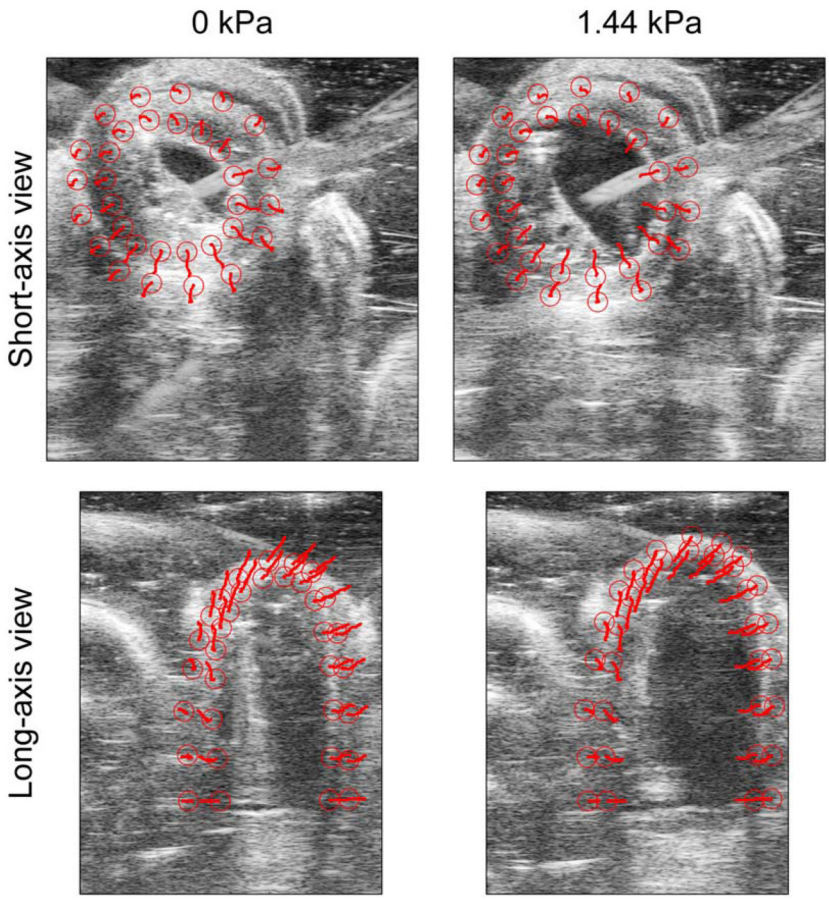

Fig. 2.

Echo recordings of a left ventricle excised from a mouse, at zero pressure (left) and passively inflated to 1.44 kPa (right). Particle paths during inflation, estimated by speckle tracking, are shown as red lines (the same paths are shown in both left and right images for reference). Red circles mark segmentation points of the inner and outer walls at the respective pressures, so that the left and right images have the starting and ending positions circled, respectively. Image dimensions are 12 mm × 11 mm (long axis) and 12 mm × 11 mm (short axis).

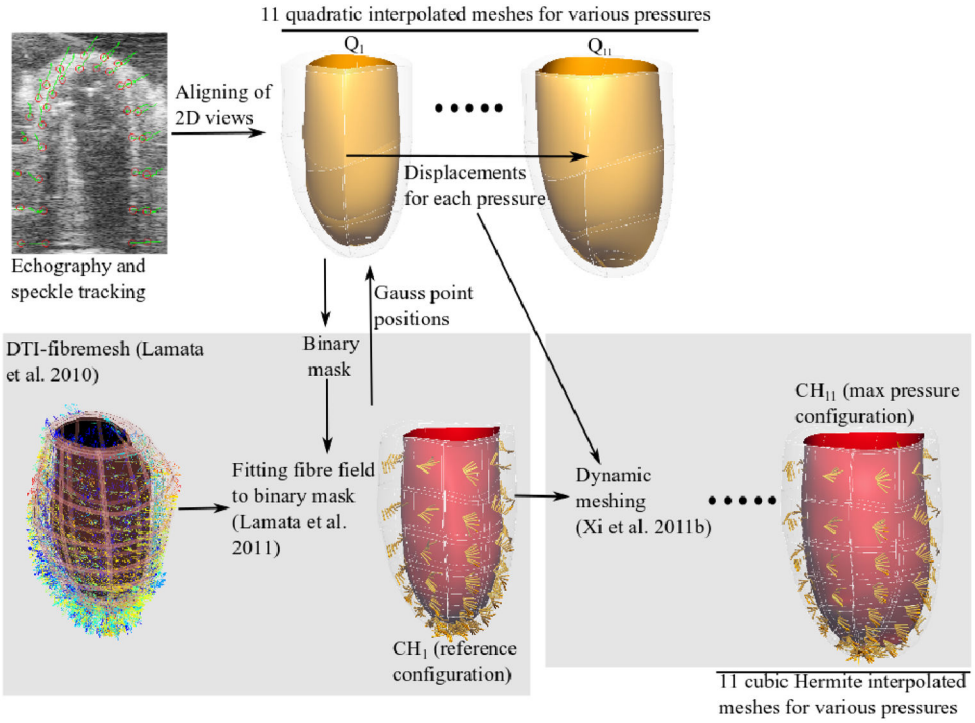

Fig. 3.

Workflow for generating cubic Hermite (CH) meshes. Material points were followed by speckle tracking from different views and aligned into quadratic interpolated meshes (Q-mesh). The zero pressure CH mesh (CH_1) was built by fitting the fibre field (yellow lines) to the binary mask of the Q-mesh corresponding to zero pressure (Q_1) [21]. Then we mapped all Gauss point positions back to Q_1 and calculated their displacements corresponding to the various pressures. These displacements were used together with the CH_1 mesh to build cubic Hermite meshes for the various pressures [24]. The CH_1 mesh was used as reference configuration for the simulation, while the other CH meshes constituted the experimental measured configurations for the various pressures

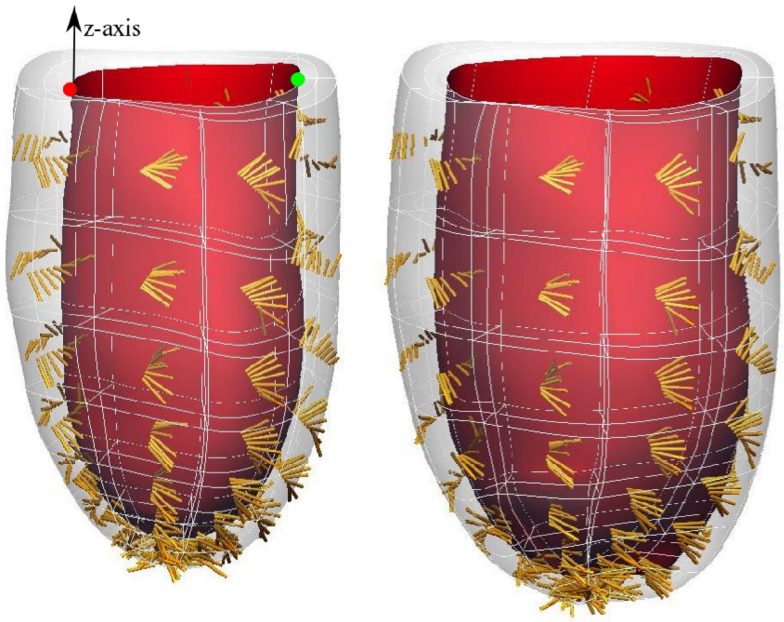

Fig. 4.

Cubic Hermite interpolated meshes of the zero pressure (left) and maximal pressure (1.44 kPa) configuration (right) based on the deformation field captured by experiments and speckle tracking. The nodes in the basal plane were constrained such that no material points contained on the basal surface were allowed to move in the z direction. The endocardial basal node at the centre of the free wall (red dot) was not allowed to move at all, while one at the middle of the septum (green dot) was only allowed to move in the radial direction. Yellow lines indicate fibre angles fitted from DTI data

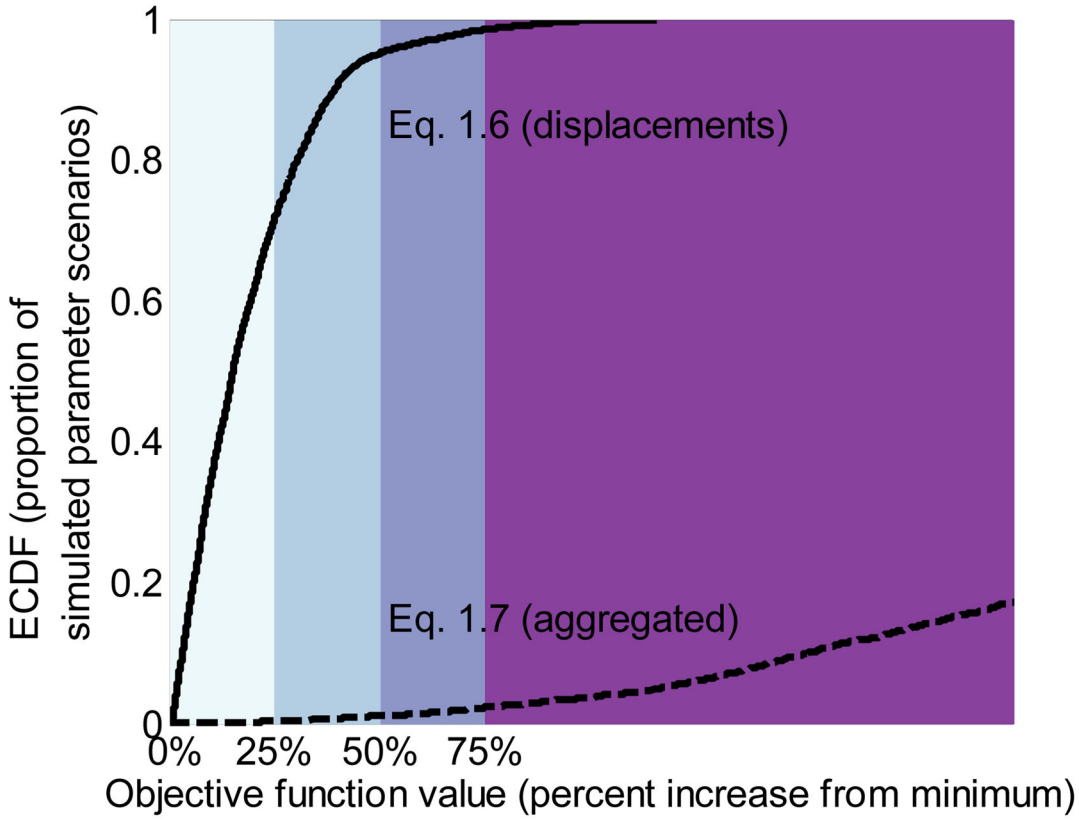

Fig. 5.

The objective function based on aggregated geometry measures (equation (7)) was more precise in identifying a narrow set of well-fitting parameter scenarios, compared to the objective function based on node displacements (equation (6)). Lines show empirical cumulative distribution functions, i.e. the proportion of simulated parameter scenarios for which the objective function was less than the value given by the horizontal axis. Color shading for the objective function value is used for comparison with Fig. 6, Fig. 7 and Fig. 8.

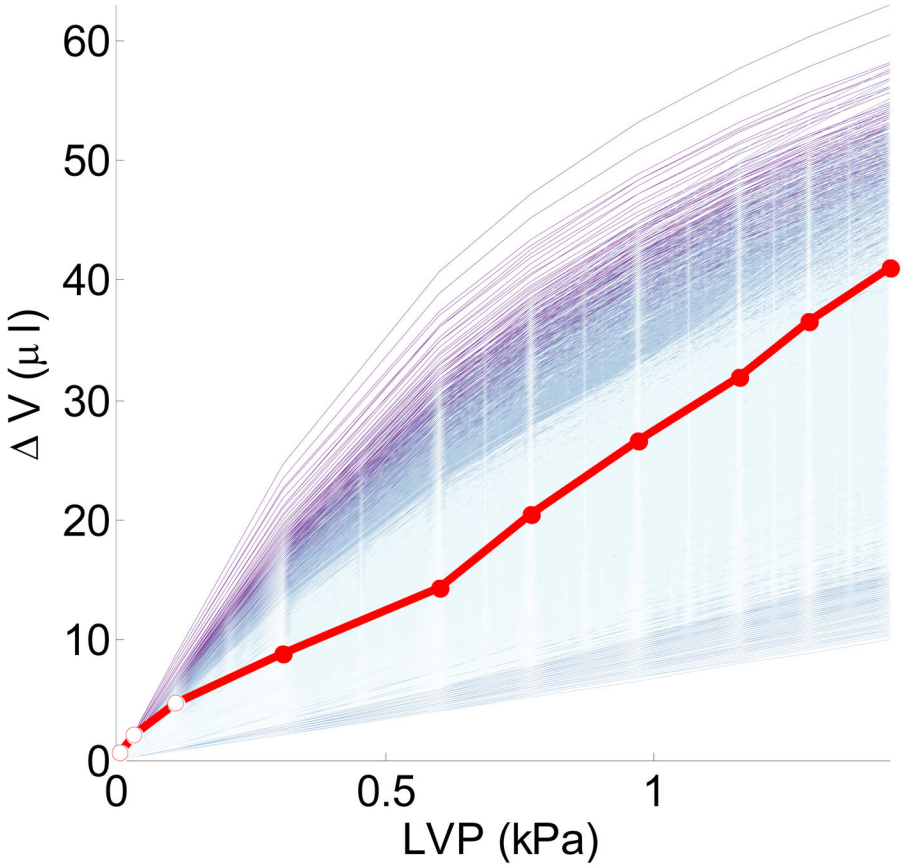

Fig. 6.

Node positions made a poor goodness-of-fit criterion (equation (6)) for matching simulations (thin lines colored with the same color scale used in Fig. 5) to observation (thick red line). Compliance is unreasonably low for many of the parameter scenarios that give low values of this objective function. Contrast with the corresponding plot (Fig. 7a) for the other objective function (equation (7)), where the best-fitting scenarios cluster more tightly around the experimental results. White dots include unphysiological pressure levels that were omitted in computing the objective function. Note that this plot shows the increase in volume as a result of imposed pressure, and so is transposed relative to the traditional P-V loop plot.

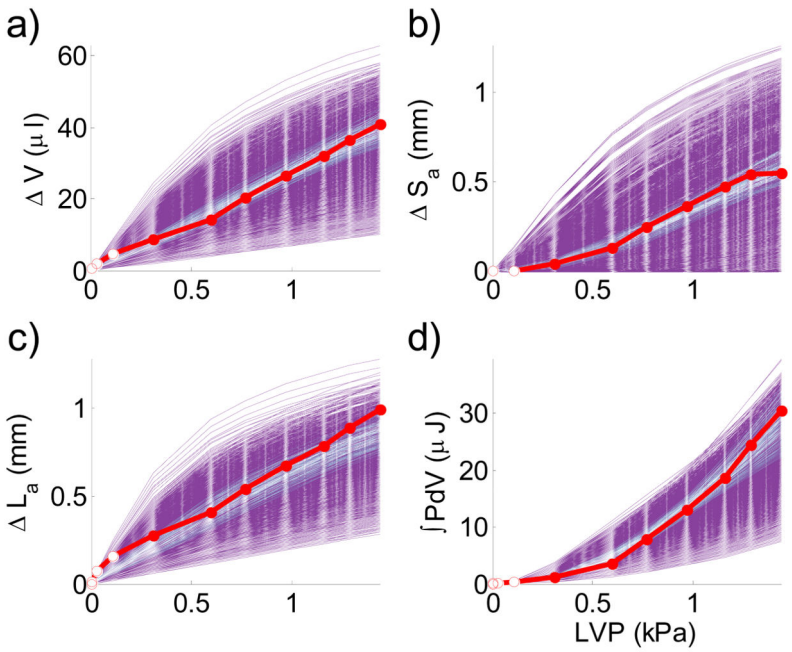

Fig. 7.

Comparison of whole-organ geometrical characteristics (see text) as a function of left ventricular pressure (LVP), between experimental data (red) and simulated data, using a goodness-of-fit measure based on whole-organ phenotypes (equation (7)). Color indicates the value of the objective function (equation (7)) relative to the minimum value (color scale as in Fig. 5 and Fig. 6). Geometric measurements are shown as differences from the zero-pressure values of volume = V_0 = 58.1 μL, long-axis diameter = LA_0 = 6.88 mm, short-axis diameter = SA_0 = 3.39 mm. Panel a) contrasts with Fig. 6. White dots indicate unphysiological pressure levels that were omitted in computing the objective function. The observed experimental relationship between pressure and volume was near-linear, in agreement with *in vivo* PV loop data (see references in text)

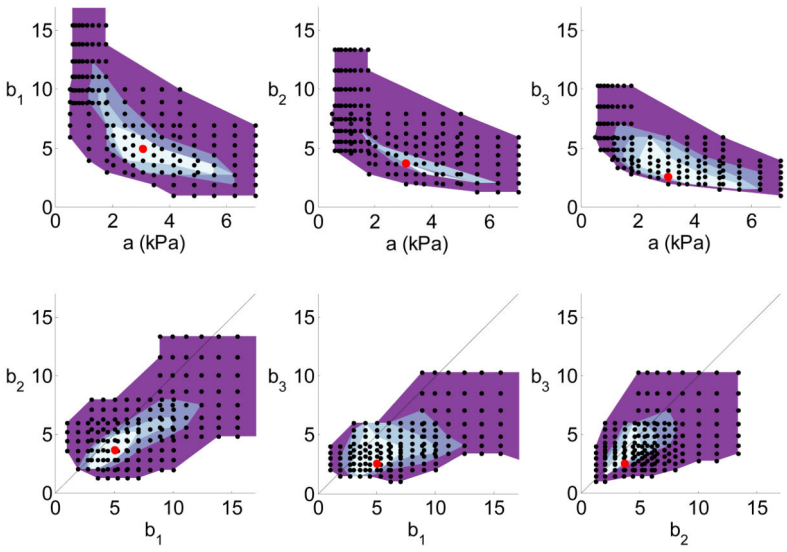

Fig. 8.

Projections of the objective function onto two-dimensional slices of the stiffness-parameter space. Each panel shows, conditional on the two parameters named on the axes, the best fit (as defined in eq. (7)) among all combinations of the remaining parameters. Black dots indicate simulated parameter sets; red dot shows the best-fitting parameter combination among the simulations. Diagonal line shows 1:1 ratio of parameters for reference. Parameter scenarios outside the displayed axis limits were also run, spanning the full parameter ranges reported in Table 1, but these did not fit well and are omitted here for clarity.

Table 1

Studies estimating the parameters in the Guccione and Costa material laws. For the current study, parentheses show the range of each parameter among scenarios that fit within a 25% increase from the minimum value of the objective function (i.e. least lack-of-fit). The Costa law is a generalization of the Guccione law, with separate coefficients for each term in the parentheses in Eq. (5). See Supplementary Figure S1 for a visualization of the stress-strain relationships corresponding to these parameter scenarios. ED=End Diastole, ES=End Systole, PV=Pressure Volume, MVO=Mitral Valve Opening

Study	Experiment	Reference Configuration	Recording	Time-points used	Species	a (kPa)	b_1	b_2	b_3
Guccione law:									
[10]*	Passive inflation	Cylinder	PV-curves, implanted markers	5	Rat Dog	2.2 2.4	9.2 26.7	2.0 2.0	3.7 14.7
[8]	Epicardial suction	Zero pressure	Tagged MRI	3	Dog	0.10–1.0	39.5–93.0	6.1–61.6	3.1–73.1
[14]	Passive inflation	Zero pressure	Tagged MRI	5	Pig	3.0	11.1	1.8	10.0
[41]	In vivo	MVO	Tagged MRI	2 (ED, ES)	Sheep	0.12–0.35	9.2–67.1	5.0–26.6	9.3–21.6
[6]	Passive inflation	Low pressure	Tagged MRI	5	Pig	0.07–0.79	8.0–83.4	6.1–36.4	8.2–62.4
[44]	In Vivo	MVO	Tagged MRI	2 (ED, ES)	Sheep	0.95	49.3	19.2	17.4
[9]*	In Vivo	MVO	Tagged MRI, pressure wire	2 (MVO, ED)	Dog	1.7	14.3	4.5	0.76
[24]	In Vivo	Zero pressure	Tagged MRI, pressure wire	2	Human	0.3	41.7	9.1	51.5
[45]	Passive inflation	Mid Diastole	PV-curves	3	Mouse	1.1	8.0	2.0	3.7
[15]*	In Vivo	Calculated	Tagged MRI, pressure wire	4–6	Human	2	19.3	10.7	12.8
Costa law#:									
[46]*	In vivo	Ellipsoid	Implanted markers	2 (ED, ES)	Dog	1.8	6.0	3.0–12.0	3.0–7.0
[47]	Shear tests	Unstressed	Tissue block	Several	Pig	0.22	42.5	7.8–18.6	10.9–11.0
[7]	Shear tests	Unstressed	Tissue block	Several	Pig	0.26	37.2	9.1–18.9	12.0
[48]	Passive inflation	Calculated	PV-curves	Several	Human	0.3	39.0	4.2–7.6	12.8–17.2
Current study	Passive inflation	Zero pressure	Echocardiography	8	Mouse	3.1 (2.0–5.6)	5.0 (2.7–7.0)	3.7 (2.1–5.2)	2.6 (1.5–6.0)

*These studies used a definition of a that was twice the one used in the other studies. Estimates in this table have been halved to make them directly comparable with the others.

#The orthotropic Costa law has three parameters in place of b_2 and two in place of b_3. The values in the b_2 and b_3 columns for Costa-law studies show the variability between these non-isotropic coefficients.